Atomic measurements of high-intensity VHF-band radio-frequency fields with a Rydberg vapor-cell detector

Eric Paradis,[1,2] Georg Raithel,[3,2] and David A. Anderson[2,3]
[1]*Department of Physics & Astronomy, Eastern Michigan University, Ypsilanti, Michigan 48197, USA*
[2]*Rydberg Technologies Inc., Ann Arbor, Michigan 48103, USA*
[3]*Physics Department, University of Michigan, Ann Arbor, Michigan 48109, USA*

(Received 9 April 2019; published 30 July 2019)

We investigate and employ optical Rydberg resonances in an atomic vapor cell for measurements of high-intensity VHF-band radio frequency (rf) electric fields. An atomic vapor cell with integrated electrodes is used to generate high-intensity 50–500 MHz rf electric fields reaching ∼5 kV/m in a submillimeter gap. The fields are measured using Rydberg electromagnetically induced transparency as an optical readout of field-sensitive $30D_J$ and $35D_J$ Rydberg states of atoms within the gap. The rf electric field is determined by matching observed spectroscopic markers, including ac level shifts, even-harmonic rf sidebands, and rf-induced avoided crossings in the Rydberg manifold to calculated spectra derived from a nonperturbative Floquet theory. In our measurements, rf field frequencies and electric-field amplitudes are determined to an accuracy of 1.0% and 1.5%, respectively. In the atom-field interaction, we observe a transition from a quantum regime, characterized by discrete even-harmonic Floquet states separated by an even multiple of the rf field frequency, into a semiclassical regime at very strong fields, in which the spectrum exhibits unresolved resonances whose strengths are smoothly modulated at a frequency of approximately five times the rf frequency. The underlying physics is explored.

DOI: 10.1103/PhysRevA.100.013420

I. INTRODUCTION

Radio-frequency (rf) electric field measurement instrumentation and standards are ubiquitously rooted in passive antenna technology [1,2]. Traditional antenna-based rf measurement technology and standards, which in their simplest form are comprised of a resistive (dipole) antenna and rectifying diode, are limited in their ability to provide accurate measurements of high-intensity rf electric fields [3]. Other significant limitations to such physical field sensors include the intrinsic presence of metallic structures that couple to and distort the incident rf field to be measured, and their physical size limited to approximately the rf wavelength, making them large and impractical for use in near-field measurement and subwavelength rf imaging applications. Further, traditional rf sensors are susceptible to short- and long-term drifts, requiring periodic calibration for which measurement uncertainties are limited to no less than ∼1 dB or ∼5% [4,5].

The advent of Rydberg-atom-based rf field measurements via electromagnetically induced transparency (EIT) in atomic vapors [6–9] present a novel alternative for rf electric field measurements [10] to traditional rf measurement technology, and a promising approach for the development of atomic rf electric field measurement standards and capabilities in rf [11–13]. Rydberg-atom-based field measurements typically employ dielectric compartments containing an atomic vapor and all-optical detection methods, avoiding the need for conducting elements within the sensing region. With this, realizing detectors with small dielectric footprints for minimal perturbation of the field becomes possible. The typical Rydberg-atom level structure further offers a wide range of resonant electric dipole transitions between Rydberg states spanning tens of MHz to sub-THz [14], and highly excited states that exhibit energy level shifts in the presence of applied ac or dc fields [15–18]. Due to this, a single atom-based sensor affords a means to performing absolute measurements of rf fields across a large rf frequency range and over a wide dynamic range in rf strength [7,19–21]. Elsewhere, Rydberg-based measurements have also been demonstrated in applications ranging from subwavelength imaging [22,23] to polarization measurements [19,24,25]. Further, Rydberg atom-based sensors preclude the need for frequent device recalibration, since the electric fields measured are derived from atomic level shifts that are directly traceable to fundamental physical constants and invariable atomic parameters.

In the present work, we use EIT [26–29] as a detection method within a rubidium vapor cell to extend high-precision rf detection measurements to high-intensity long-wavelength rf fields and demonstrate continuous-frequency rf electric field measurement across the entire VHF band. A pair of closely spaced parallel electrodes integrated into a vapor cell [30] generate high-intensity rf test fields in the optically accessed atomic-vapor detection volume. The EIT readout from rubidium Rydberg states $30D_{3/2,5/2}$ and $35D_{3/2,5/2}$ are compared to theoretical models to yield the applied electric field in absolute units. In recent work, 50 and 100 MHz rf fields have been measured to ∼300 V/m [8,31] and recently K_a band rf field measurements to ∼1 kV/m field levels [19]. Here, the rf field measurement capability is extended by nearly an order of magnitude, to fields >5000 V/m and full VHF-band coverage, with rf fields varying continuously from 50–500 MHz. Electric fields are determined by a method comparing experimentally measured spectra to state-level calculations performed using a nonperturbative Floquet approach [10,29] to include the effects of high-order level shifts, state

 ©2019 American Physical Society

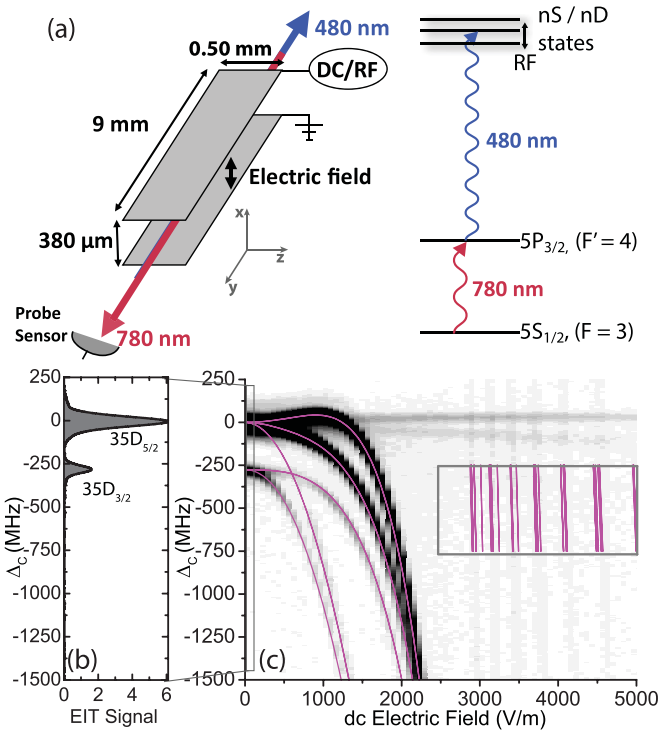

FIG. 1. Experimental setup and electrode characterization. (a) A 780 nm probe laser beam (FWHM ∼70 μm) resonant with the $5S_{1/2}$, $F = 3$ to $5P_{3/2}$, $F' = 4$ transition for ^{85}Rb is counter-propagated with a 480 nm coupling laser beam (FWHM ∼70 μm) through a Rb vapor cell. Electrodes inside the cell and wire feed-throughs allow for application of ac and dc electric fields. The EIT level scheme is shown on the right. (b) Change in probe transmission signal on the 5*S*-5*P* lower transition, exhibiting EIT (horizontal axis) as the frequency of the 480 nm beam is swept across the 35*D* Rydberg resonance (vertical axis). (c) dc-field Rydberg spectroscopy. The coupling laser is repeatedly scanned over a range of about 2 GHz (coupling laser detuning Δ_c on vertical axis), while the dc voltage difference applied to the electrodes is stepped from scan to scan to probe an electric-field range from 0–5 kV/m (horizontal axis). The scans are combined to form a map of the 35*D* state versus applied electric field. At electric fields $\gtrsim$3 kV/m the linear Stark states belonging to the $n = 34$ manifold of states become visible. The overlay of solid magenta lines shows the result of a Stark map calculation.

mixing, and multiphoton resonances [32]. To obtain further insight into the underlying physics, we present a semiclassical model that is useful for strong rf fields with frequencies below about 100 MHz. The recorded EIT spectra provide accurate absolute frequency and intensity measurements of rf fields.

II. EXPERIMENTAL SETUP AND METHODS

Figure 1(a) shows the experimental setup. The vapor cell is an elongated glass cell with internal cross section of 10 × 10 mm. Two planar steel electrodes of 9 mm length, 0.5 mm width, and 3 mm thickness are separated by a narrow gap of width $d = 380 \pm 15$ μm, capable of producing electric fields exceeding 10 kV/m for an applied voltage difference of 5 V between the plates. Figure 1(a) illustrates the photocoupling to the Rydberg states by electromagnetically induced transparency (EIT). The EIT signal is generated by a standard three-level ladder scheme [33] in ^{85}Rb. Two narrow-linewidth (<1 MHz) laser beams with a full width at half maximum (FWHM) of the intensity profile of 70 μm are counterpropagated through the gap between the two parallel electrode plates. The lasers are linearly polarized normal to the electrode planes. The 780 nm beam (probe beam) is frequency stabilized to the ^{85}Rb $|5S_{1/2}, F = 3\rangle \rightarrow |5P_{3/2}, F' = 4\rangle$ transition. The probe beam is propagated through the vapor-cell electrode gap, and its absorption through the vapor monitored on a photodiode while the 480 nm beam (coupling beam) is overlapped and counterpropagated through the same channel, and its frequency scanned linearly over ∼2 GHz across chosen Rydberg resonances. At the beam centers, the coupling transition Rabi frequencies for the $5P_{3/2}$ to 30*D* and 35*D* states are $\Omega_{30D} \simeq 2\pi \times 26$ MHz and $\Omega_{35D} \simeq 2\pi \times 21$ MHz, respectively, and $\Omega_{5P} \simeq 2\pi \times 17$ MHz for the probe $5S_{1/2}$ to $5P_{3/2}$ transition (decay rate $\Gamma_{eg} = 2\pi \times 6$ MHz). In the presented data, the frequency scan of the coupling beam is linearized using transmission peaks of an independent, temperature-stabilized Fabry-Pérot cavity and referenced to the field-free Rydberg-level energy. The change in probe transmission signal through the vapor cell is recorded; this increases when the coupling beam becomes resonant with any of the Rydberg resonances, which shift and split in response to the applied rf field. The resulting EIT spectra are used to investigate the Rydberg-atom response to the high-intensity rf electric fields, and from there to obtain measurements of the rf field amplitude and frequency by comparing the readout spectra to precalculated atomic reference spectra [10].

In the present vapor-cell experiment the atom field interaction time is below 1 μs, so blackbody-induced thermal decay of the Rydberg atoms do not contribute to the spectroscopic readout for field measurements using the states investigated here. We have calculated 300 K lifetimes of 22 μs for 30*D*, and 35 μs for the 35 state. Further, due to our moderate cell temperature and atom density, low laser powers and low principal quantum numbers, free ion charges are not anticipated to play a role in the measurements.

In dc electric fields the fine structure coupling is broken up and ℓ-state degeneracies become lifted, and the levels become recoupled into Stark states that exhibit approximately quadratic shifts in weak and linear shifts in strong fields [14]. In the case of strong ac electric fields, even-order harmonics of the applied frequency emerge [34] and produce a complex set of rf modulation sidebands with ac shifts and (anti)crossings [8].

In our experimental demonstration, dc and rf electric fields are applied to one electrode while the other is explicitly grounded. A differential probe absorption signal is recorded. To increase the sensitivity, the 480 nm coupling laser amplitude is square-wave-modulated at a repetition rate of ∼20 kHz and demodulated by a digital lock-in amplifier prior to recording. The vapor cell is temperature stabilized to ∼50 °C to increase the atomic vapor density and EIT signal to noise ratio. The relative reduction in optical transmission, i.e., the absorption, will scale with the vapor pressure, and thus increase exponentially with absolute temperature. Under our experimental conditions, a single EIT trace for a fixed rf

electric field as shown in Fig. 1(b) is typically recorded on a timescale of approximately 1 s, dictated by the chosen range of the coupling-laser frequency scan and the lock-in amplifier modulation rate. The data presented here is an average of 20 individual traces.

In the theoretical component of our work, we employ a Floquet method to calculate the response of the Rydberg atoms to strong rf fields. The Floquet method is a nonperturbative approach whose application to Rydberg-EIT spectroscopy and rf field sensing and measurement has been established in earlier work [10,29]. Here, the Floquet treatment allows us to quantify the accuracy and precision with which high-intensity VHF-band rf fields may be determined from spectroscopic Rydberg EIT readout from the electrode-integrated vapor cell. In our Floquet calculation we use basis sets $|n, \ell, J, m_J\rangle$, with m_J being fixed at 1/2 or 3/2, and a range of the effective principal quantum number ($26.05 < n_{\rm eff} < 30.95$), and all allowed ℓ and J values included. The $m_J = 1/2$ calculations include a total of 229 electronic states, and the $m_J = 3/2$ calculations a total of 219 electronic states. The number of rf photons involved in the calculated excitations ranges up to ± 10.

At the highest rf fields investigated in our work, we observe a near-periodic spectral modulation of the strengths of unresolved, dense sets of Floquet states. These spectral modulations are distinct from the usual low-field rf sidebands [8,9,34] in that they result from a periodic modulation of the excitation strength on a dense quasicontinuum of rf-mixed hydrogenic ($\ell > 3$) states. A semiclassical approximation is introduced to explain the observed modulations in this novel regime.

III. RESULTS

A. dc field calibration

We examine the EIT signal in dc electric fields to calibrate the electrode gap size. A baseline EIT spectrum of the $35D_{3/2}$ and $35D_{5/2}$ fine structure resonances is shown in Fig. 1(b), using the field-free fine structure splitting (279.64 MHz) as a frequency reference. The FWHM widths of the 3/2 and 5/2 peaks in Fig. 1(b) are are $2\pi \times 52$ and $2\pi \times 66$ MHz respectively, consistent with the Rabi frequencies stated in Sec. II [35,36]. The large optical Rabi frequencies allow for observation of weak EIT lines in the strong field regime where the oscillator strength is spread across an increasing number of Rydberg levels. The electrode structure was initially degaussed to remove any unwanted magnetization, and separate low-intensity EIT traces with narrow line widths gave an upper bound of 2 Gauss to the magnetic field within the probing region. Figure 1(c) shows an experimental dc Stark map of the Rb $35D$ lines up to 5000 V/m. The calculated Stark resonances are shown as thin solid lines overlaying the experimental signal. The atomic dc electric field measurement is obtained by matching the measured spectra to the calculated Stark structure. This agrees to within 3% with the expected field as determined from the measured gap size d and voltage V_{dc}. The lower stability limit for applied electric fields is of 3 V/m, corresponding to an applied voltage of 1 mV. The EIT resonances begin to exhibit significant broadening (>10%) at electric field levels of $E \sim 800$ V/m. Since the transverse width of the probing region is 70 μm, some field inhomogeneity is expected due to the narrow width (0.5 mm) of the electrode plates. Careful alignment and centering of the probe/coupling laser overlap region between the electrode plates is required to minimize this signal broadening. Moreover, the excitation region extends ~0.5 mm on each side past the electrode plates to the vapor-cell wall, where the electric field diminishes and appears to be further reduced by migration of free charges onto the glass wall [8,9,28]. This manifests in an observed small EIT signal with nearly vanishing Stark shifts throughout Fig. 1(c). At a field of about 1000 V/m, the system progresses into the electric-field-dominant regime, where the fine structure states are decoupled into resonances with approximately conserved m_ℓ and m_s. Under strong-field conditions (3000–5000 V/m), weak EIT signals induced by ℓ mixing with linear hydrogenic Stark states (where $\ell > 3$) are observed. The inset box in Fig. 1(c) shows the calculated linear, hydrogenic Stark resonances (cropped to allow for visual comparison).

B. Rydberg-EIT spectra in strong ac fields

Modulation of the EIT signal in a strong rf field up to $E_{rf} \sim 10$ kV/m is shown in Fig. 2, as the coupling laser is scanned across the $30D_{3/2}$ and $30D_{5/2}$ Rydberg resonances (fine-structure splitting 452.40 MHz). An ac voltage of frequency $\nu_{rf} = 50$ MHz is injected into a linear amplifier with 40 dB gain, and the output is applied across the vapor cell electrodes. The power injected into the amplifier is fixed for each vertical trace, and increased for successive measurements in steps of 0.25 dB. The amplitude of the rf electric field, E_{rf}, defines a local rf field intensity, $I = (1/2)c\epsilon_0 E_{rf}^2$, which we then express on a dBI scale. The dBI value is given by $10 \times \log_{10}(I/I_0)$, where $I_0 = 1$ W/m^2. The absolute dBI value of the rf intensity, used in the Floquet calculations (red and blue symbols in Fig. 2), is related to the known rf power applied in the experiment, given in units of dBm, via $dBI = dBm + \text{const}$. The constant is obtained by an empirical match of the experimental to the calculated data. For reference, $I = +45.2$ dBI corresponds to an applied peak electric field amplitude of $E_{rf} = 5000$ V/m. The matching process amounts to an atom-based calibration of the rf transmission system, and an atom-based measurement of the rf electric field present in the cell. While in the present demonstration the field measurement is performed with an applied rf test field, the method is equally applicable in ambient rf fields incident from remote transmitters.

As the injected rf power is increased, rf sidebands at even multiples of $\nu_{rf} = 50$ MHz emerge due to absorption or emission of photon pairs from the rf field. As the field contains no dc component, following parity conservation no odd harmonics are observed [34]. Individual resonances and rf sidebands remain relatively narrow (~70 MHz FWHM) until $I \gtrsim 42$ dBI, where the rf field becomes strong enough to cause mixing with hydrogenic Stark states. In Fig. 2(b) we show rf harmonics at $I = 41.5$ dBI. There, six peaks corresponding to even rf sidebands of the dominant ac-Stark-shifted line are clearly visible, showing an average spacing of 99 ± 4 MHz, in agreement with the expected spacing of $2\nu_{rf}$.

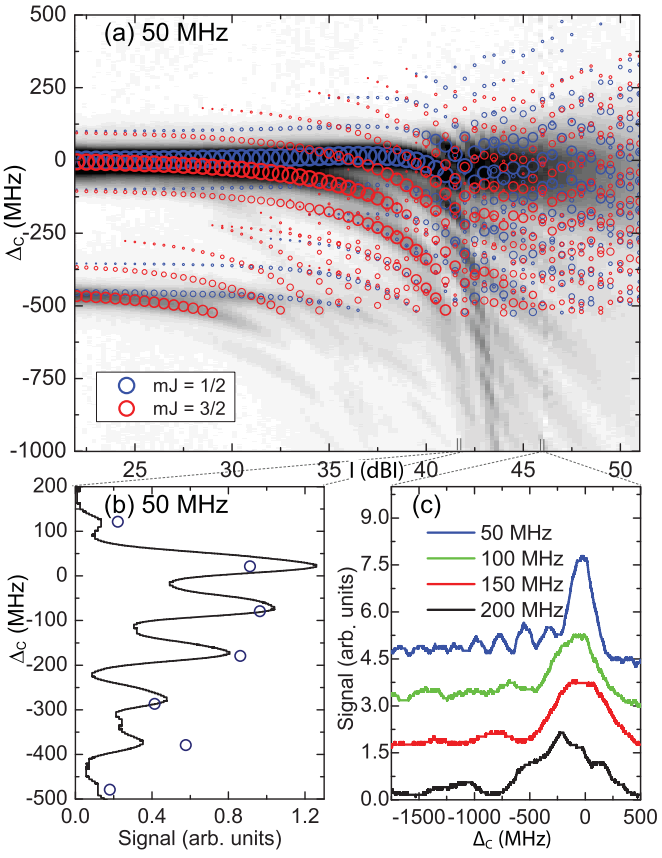

FIG. 2. (a) Measured $30D_{3/2}$ and $30D_{5/2}$ EIT resonances over the indicated range of the coupling laser detuning Δ_c (vertical axis) and the rf intensity I given in dBI (horizontal axis), in an applied rf field with frequency of $\nu_{rf} = 50$ MHz. The measured signal refers to the change in probe transmission through the cell, and $\Delta_c = 0$ corresponds to the field-free $30D_{5/2}$ state resonance. As the intensity I is increased, even harmonics shifted by $2n\nu_{rf}$ from the parent line emerge (integer n). The overlaid blue and red circles represent signal strengths from Floquet calculations for $m_J = 1/2$ and $m_J = 3/2$, respectively. (b) A single cut at 41.5 dBI shows six harmonic peaks with average spacing of 99 ± 4 MHz $= 2\nu_{rf}$. Circles correspond to calculated relative signal strength peaks, summed over the $m_J = 1/2$ and $m_J = 3/2$ states. (c) Single cuts taken under strong field conditions (+46 dBI), for various applied rf frequencies. In this regime, unresolved lines are modulated by a periodic envelope function with a periodicity of $\sim 5\nu_{rf}$.

At intensities >42 dBI mixing with the hydrogenic manifold is observed, leading to an abundance of Rydberg energy levels and rf sidebands that overlap with each other in the recorded spectra. Figure 2(c) shows single scans at +46 dBI for four different rf frequencies. It is evident that individual EIT resonances can no longer be resolved. However, the level-averaged line strength develops a clear periodic modulation pattern, with a periodicity of about $5\nu_{rf}$. In contrast to the rf modulation sidebands of resolved EIT lines in weak rf fields, whose spacing is quantized at $2\nu_{rf}$, the periodicity of the high-field structures does not appear to be quantized in exact integers of ν_{rf}, and it varies as a function of Δ_c and rf field intensity. In the following we use a semiclassical model to explain the physical origin of these high-field modulations.

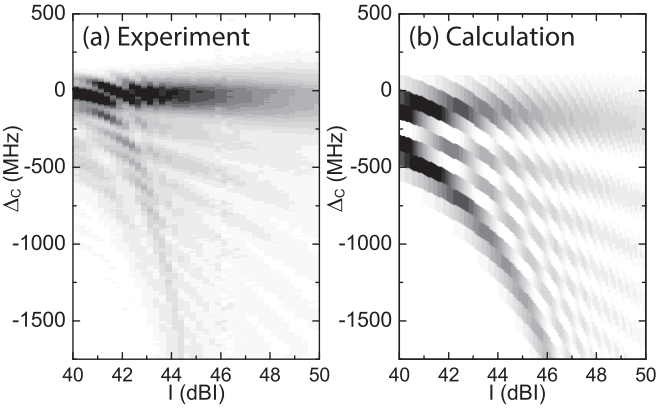

FIG. 3. (a) Measured high-field EIT spectra over the indicated range of the coupling laser detuning Δ_c (vertical axis) and the rf intensity I given in dBI (horizontal axis), for the $30D_{3/2}$ and $30D_{5/2}$ states and $\nu_{rf} = 50$ MHz. $\Delta_c = 0$ corresponds to the field-free $30D_{5/2}$ state resonance. (b) Corresponding EIT signal strength calculated according to the semiclassical Eq. (1).

The essential physics of the smooth modulation pattern observed in strong rf fields is captured by considering a D-type Rydberg level that exhibits an ac shift of $-(\alpha/4)E_{rf}^2$, with an ac polarizability α that is close to the dc one (which is a good assumption at the low rf frequencies considered here). The position of the nth order rf sideband (even integer n) is then given by $\Delta_c = -(\alpha/4)E_{rf}^2 - n\,h\nu_{rf}$ [34]. For a low value of ν_{rf} and relatively large EIT linewidth there are many rf sidebands, constituting a spectrum with a fairly high density of states [see Fig. 2(a) above about 40 dBI]. At the same time, in high-rf fields the oscillator strengths of the D-character lines and their rf sidebands spread somewhat into a dense background of hydrogenlike levels that intersect with the D lines [see Fig. 2(a) above about 43 dBI]. As a result, in high fields we expect a quasicontinuum of states with shifts $\Delta_c = -(\alpha/4)E_{rf}^2 - nh\nu_{rf}$. The average oscillator strength of these states, $S(\Delta_c)$, is given by

$$S(\Delta_c) \approx \left| \mathrm{J}_{m(\Delta_c, E_{rf})} \left[\frac{\alpha E_{rf}^2}{8h\nu_{rf}} \right] \right|^2 \qquad (1)$$

with a Bessel function order $m = \frac{\Delta_c}{2\nu_{rf}} + \frac{\alpha E_{rf}^2}{8h\nu_{rf}}$. Since ν_{rf} is small, for the ease of computation we may approximate m with its nearest integer value. In effect, Eq. (1) allows us to compute a spectrum on the Δ_c-I plane (with intensity I dependent on E_{rf} and given in dBI). In Fig. 3 we compare the result of this calculation with equivalent experimental data. There is a surprising level of agreement, given the simplicity of the semiclassical calculation. Even the moiré pattern that results from the intersection of two types of modulation stripes is captured quite well. Minor disagreement is attributed to the fact that the ac Stark shift of the D lines only approximately follows a trend given by $-(\alpha/4)E_{rf}^2$.

C. Dependence on ac field frequency and avoided crossings

In the following, we provide a detailed discussion of the case of resolved rf sidebands and Rydberg transitions.

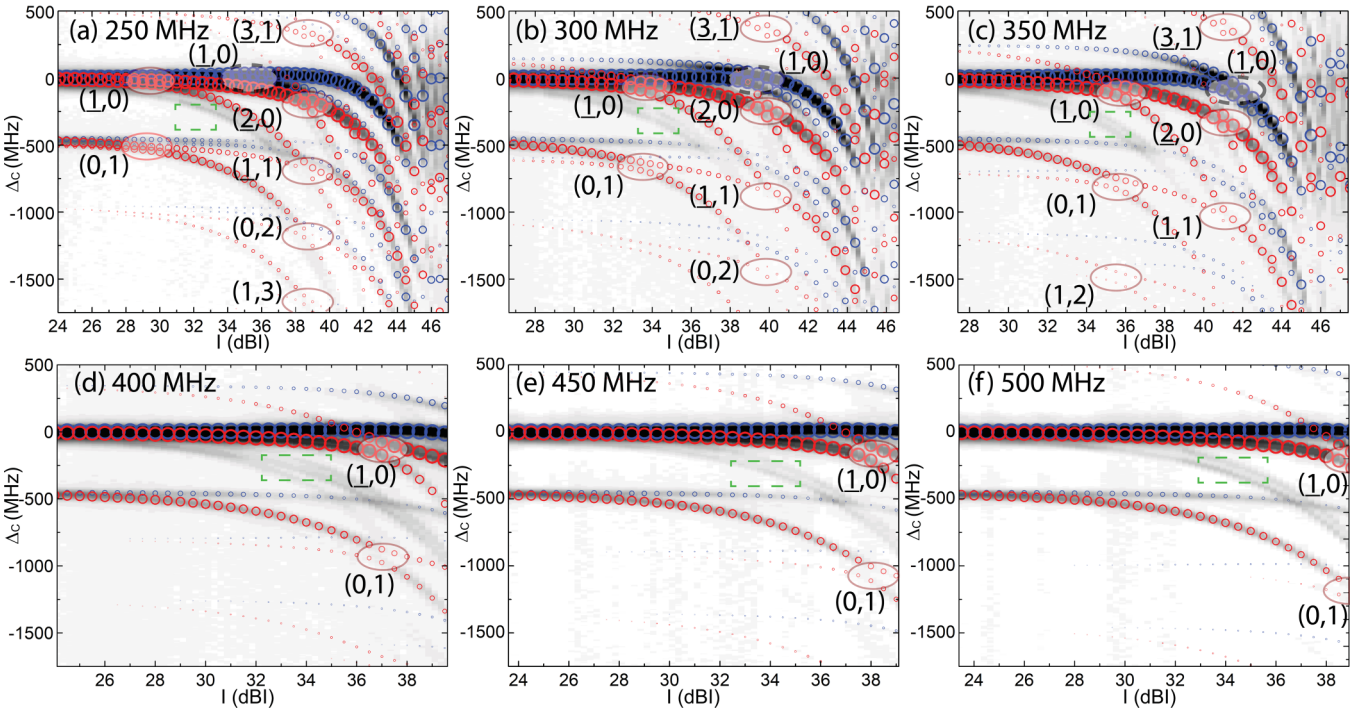

FIG. 4. EIT spectral maps of the 30D Rydberg state for the indicated values of ν_{rf} and intensity ranges (horizontal scale). The probe frequency is locked, and the coupling-laser frequency detuning Δ_c is scanned (vertical scale). The overlays of blue and red circles represent calculated Floquet spectra for $m_J = 1/2$ and $m_J = 3/2$ sublevels, respectively. Several avoided crossings are highlighted (labels explained in text).

Figure 4 shows a set of plots for ν_{rf} ranging from 250–500 MHz. A calculated Floquet map is overlayed atop each set of experimental data. Blue and red circles correspond to $m_J = 1/2$ and $m_J = 3/2$ sublevels, respectively; the cross-sectional areas of the circles are proportional to the calculated excitation rates of the Floquet levels. We observe excellent agreement between calculated and observed level shifts, as well as good qualitative agreement in relative line strengths. For rf fields $E_{rf} \sim 5000$ V/m, corresponding to $I \sim 45$ dBI, the calculation allows for a calibration of E_{rf} to within $\pm 1.5\%$. This error estimate is obtained by comparing frequency offsets between calculated and measured transition peaks in the spectral maps, and extracting the variance in electric-field values that would produce such offsets.

In Fig. 4, several avoided crossings are marked within the experimental resonance maps. In the absence of dc electric fields, all levels in the spectrum studied here have a fixed atomic angular momentum, $\ell = 2$. Due to the parity rules for electric-dipole transitions, only rf couplings are allowed that involve even numbers of rf photons. The coupling laser frequencies at which the $J = 3/2$ and $J = 5/2$ rf bands are excited are

$$\begin{aligned} \Delta_{c,3/2} &= W_{3/2}/h - 2n\nu_{rf} \\ \Delta_{c,5/2} &= W_{5/2}/h - 2m\nu_{rf}, \end{aligned} \tag{2}$$

where W_J are bare atomic energy levels, and n and m are respective numbers of rf photon pairs that become absorbed while the Rydberg atom is laser excited. Avoided crossings occur when two rf bands with the same m_J, one belonging to a $J = 3/2$ and the other to a $J = 5/2$ state, intersect. Since rf-induced coupling between the two intersecting levels is allowed in an even order by the electric-dipole selection rules, these intersections form avoided crossings. The rf bands forming the avoided crossings marked in Fig. 4 are identified by the numbers (n, m) defined in Eq. (2). In Fig. 4, underlined numbers are negative and correspond to rf photon emission. Since at the anti-crossings it is $\Delta_{c,3/2} = \Delta_{c,5/2}$, the energy difference between the bare, ac-shifted atomic states at the anticrossings is given by

$$W_{5/2} - W_{3/2} = 2h\nu_{rf}(m - n). \tag{3}$$

For example, there is a pair of avoided crossings in the 400 MHz map, in the bottom left panel of Fig. 4. The intersecting bands at the upper avoided crossing, denoted $(\underline{1}, 0)$, are a $30D_{3/2}$ $m_J = 3/2$ band that involves the emission of two rf photons concurrent with laser excitation, signified by the number $n = -1$, and a $30D_{5/2}$ $m_J = 3/2$ band that involves no rf photons, signified by the number $m = 0$. According to Eq. (3), in this case the difference between the ac-shifted bare atomic energy levels is $W_{5/2} - W_{3/2} = 2h\nu_{rf} = h \times 800$ MHz. Essentially, the emission of two rf photons concomitant with the excitation of the $30D_{3/2}$ level raises the laser excitation frequency by 800 MHz, bringing it into resonance with the laser excitation frequency of the $30D_{5/2}$ level with no rf photons absorbed or emitted. Similarly, at the avoided crossing labeled (0,1) one pair of rf photons is absorbed while exciting the $30D_{5/2}$ level, lowering the $30D_{5/2}$ laser excitation frequency by 800 MHz and bringing it into resonance with the laser excitation frequency of the $30D_{3/2}$ level with no rf photons absorbed or emitted.

In Fig. 4 there exist a few weak, experimentally observed bands that are not accounted for in the Floquet calculation. These are due to two distinct phenomena. First, a nonzero velocity class of atoms in the vapor cell couples to the Rydberg states through the intermediate-state hyperfine sublevel $|5P_{3/2}, F' = 3\rangle$, which is 120 MHz below the $F' = 4$ level (which is resonant with the probe laser at about zero velocity). This produces faint Doppler-shifted copies of the EIT resonances 75 MHz below the main resonances (the shift is 120 MHz times a Doppler factor of 780 nm/480 nm − 1, with probe and coupling wavelengths 780 nm and 480 nm). Second, the laser polarizations are perpendicular to the electrode planes to within a few percent. Polarization imperfection allows for the observation of $30D_{5/2}$ $m_J = 5/2$ bands; these are visible in Fig. 4 just below the strongest resonance, indicated by the small dashed green rectangle for each plot.

D. ac shifts and avoided-crossing gaps

For an avoided crossing labeled (n, m) as described in the previous section, the coupling at the avoided crossing is an electric-dipole coupling in Nth order between fine-structure levels of the same ℓ and different J, with an $N = 2|m - n|$. Hence, certain scalings of the gap size are expected. Further, including the ac shift of the transition, Δ_{ac}, which in our case is positive and depends strongly on rf intensity and only weakly on ν_{rf}, the resonance condition at which the crossings occur is $2\nu_{rf}(m - n) = \Delta_{ac} + \Delta_{FS0}$, where Δ_{FS0} is the field-free fine structure splitting. In this section, these dependencies are discussed.

First, we note that crossings labeled $(n + k, m + k)$ for fixed integers n and m and varying integer k all occur at the same rf intensity. In Fig. 5(a) we verify that the distances between avoided crossings (n, m) and $(n + k, m + k)$ on the Δ_c axis are given by $2k\nu_{rf}$. In the figure we show frequency spacing between the pair of avoided crossings $(\underline{1}, 0)$ and (0,1), for $m_J = 3/2$, as a function of ν_{rf}. Such a pair of avoided crossings will occur at a given applied intensity value, that increases as a function of ν_{rf}. Since for this pair of avoided crossings $k = 1$, the coupling laser frequency spacing between these avoided crossings is always $2\nu_{rf}$, regardless of the exact intensity value at which the avoided crossings occur. A linear fit gives a slope of 1.99 ± 0.05 with intercept 7 ± 22 ($r^2 = 0.997$). Figure 5(a) and similar studies of other anticrossings in Fig. 4 show that measurement of the avoided-crossing distances on the Δ_c axis can be used to obtain a rf frequency measurement accurate to within 1% of the incident rf frequency value.

In Fig. 5(b) we investigate the gap sizes of the observed avoided crossings versus the rf electric field strength. As the avoided crossings are due to $E1$ couplings of order $2|n - m|$, one may expect the avoided-crossing gap sizes to scale with E_{rf} to the power $2|n - m|$. This scaling would only hold if the Floquet states were invariant with respect to E_{rf}. The observed avoided-crossing coupling strengths do increase with electric field, but only in an approximately linear fashion for the $2|n - m| = 2$ cases and only about quadratic for the $2|n - m| = 4$ case. Also, at the highest fields the coupling strengths tend to level out. These observations indicate that with increasing E_{rf} the intersecting Floquet states undergo a significant increase in state mixing. This likely causes the weaker-than-expected scaling of gap size vs E_{rf}.

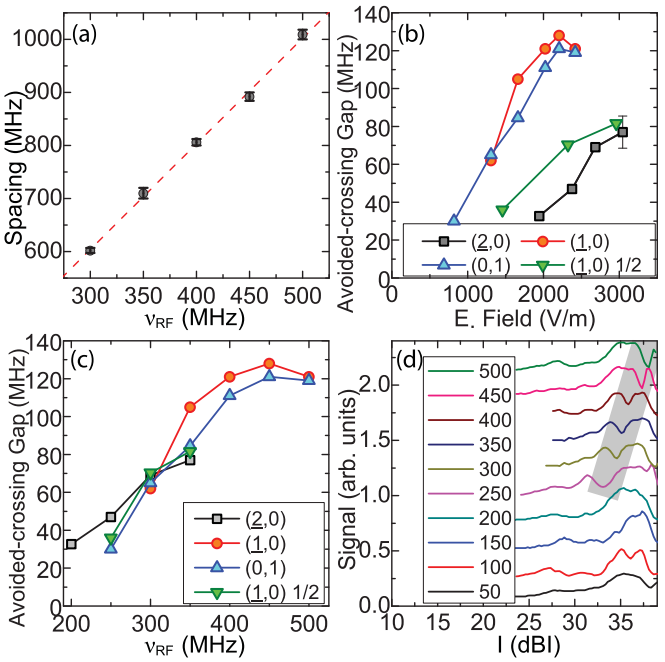

FIG. 5. Effect of applied rf frequency on $30D$ Rydberg levels. (a) Frequency separation between $m_J = 3/2$ (1,0) and (0,$\underline{1}$) avoided-crossings versus rf frequency. A linear fit (dashed line) gives a slope of 1.99 ± 0.05 ($r^2 = 0.997$). (b) Measurement of the gap size versus applied electric field (V/m), for observed avoided crossings. All avoided crossings are of $m_J = 3/2$, except for the inverted triangles ($m_J = 1/2$). (c) Measurement of the avoided-crossing gap size versus applied rf frequency. (d) Change in probe beam transmission signal showing EIT versus intensity (dBI) at a fixed frequency of −100 MHz (relative to the $30D_{5/2}$ zero-field resonance), for various applied rf frequencies (MHz). The highlighted region shows the $m_J = 3/2$ $(\underline{1}, 0)$ avoided crossing shifted up in dBI for increasing rf frequency.

In Fig. 5(c) we plot avoided-crossing gap sizes vs. ν_{rf}. The avoided-crossing gaps rapidly increase with ν_{rf}. This is due to the facts that the field-free fine-structure splitting of $30D_{5/2}$ and $30D_{3/2}$ is $\Delta_{FS0} = 452$ MHz, and that the splitting increases with E_{rf} due to ac shifts. With increasing ν_{rf}, stronger rf electric fields are required to ac-Stark-shift rf sidebands of states with different J into resonance with each other. Stronger rf electric fields, in turn, correspond with larger avoided-crossing gap sizes. For the highest values ν_{rf} that were investigated, the gap sizes tend to level out. This observation is attributed to increased state mixing in stronger E_{rf} fields. We also observe that for given ν_{rf} the displayed avoided crossings show approximately the same gap size.

Finally, in Fig. 5(d) we pick a fixed frequency of 100 MHz below the $30D_{5/2}$ field-free energy level, and plot the EIT signal versus rf intensity I in dBI, for a range of rf frequencies ν_{rf}. As the intensity increases, several $m_J = 3/2$ levels come into resonance due to their increasing ac shifts, while, over the intensity range shown, the $m_J = 1/2$ levels remain out of view. As over the entire ν_{rf} range studied the ac polarizability remains close to the dc polarizability, the overall

coarse structure of the curves is similar for all ν_{rf} values. The avoided-crossing structure discussed in Sec. III C does, however, depend on ν_{rf} and leads to variations among the curves in Fig. 5(d). In particular, the $(\underline{1}, 0)$ avoided crossing for $m_J = 3/2$ manifests as a notch that moves through the curves as the rf frequency is changed (highlighted region). For increasing rf power the 30*D* fine-structure gap ac shifts from $\Delta_{FS0} = 452\,\text{MHz}$ to about 1 GHz, due to the increasing ac shift of the transition Δ_{ac}. Hence, with increasing rf frequency the $(\underline{1}, 0)$ avoided crossing occurs at increasing intensity levels, as larger values of Δ_{ac} are needed to tune the states into the two-photon rf resonance $2\nu_{rf} = \Delta_{ac} + \Delta_{FS0}$. The notch indicative of the $(\underline{1}, 0)$ avoided crossing is absent for frequencies below 250 MHz. This is because $\Delta_{ac} > 0$, and therefore the two-photon resonance $2 \times \nu_{rf} = 452\,\text{MHz} + \Delta_{ac}$ cannot be met for $\nu_{rf} < 226\,\text{MHz}$.

IV. CONCLUSION

We have employed vapor-cell EIT measurements to investigate rubidium 30*D* and 35*D* Rydberg atoms in dc and ac electric fields >5000 V/m, which exceeds earlier studies by nearly an order of magnitude in field strength [8,9,31,34]. Vapor-cell high-intensity field measurements were performed using a pair of cell-integrated parallel-plate electrodes to generate near homogeneous electric fields, with no significant inhomogeneous line broadening observed in fields $\lesssim$800 V/m. The spectroscopic response to rf fields was mapped over a continuous rf frequency range spanning the entire VHF band from 50 to 500 MHz. The measured strong-field spectral maps are in excellent agreement with Floquet calculations. Additional insight into the high-field modulation behavior of the atomic spectrum was obtained by introducing a semiclassical model for the atom-field response in this strong-field regime. Avoided crossings between Floquet states were categorized using the numbers of rf photons involved in the crossings, and the scaling of observed avoided-crossing gap sizes was explored. Comparing measured spectra to the reference calculations, absolute rf frequencies and field strengths have been extracted with an uncertainty of $\pm 1.0\%$ and $\pm 1.5\%$, respectively, for fields up to 5000 V/m. In the present implementation, the dynamic range is limited at the high end by the available rf power, whereas at the lower end of the range it is limited by the minimum measurable shift of the spectroscopic line, dictated by the EIT linewidth in our experimental conditions. In the present case this corresponds to a 25 dB dynamic range. Future work may be directed at increasing the dynamic range, and at further miniaturization of vapor-cell detectors. Technical challenges in scalability may include limiting the effects of internal electric fields and avoiding temperature-dependent dielectric surface charge accumulation.

ACKNOWLEDGMENTS

This work was supported by Rydberg Technologies. G.R. acknowledges support from the NSF (Grants No. PHY-1806809 and No. PHY-1707377). This material is based upon work supported by the Defense Advanced Research Projects Agency (DARPA) and the Army Contracting Command-Aberdeen Proving Grounds (ACC-APG) under Contract No. W911NF-17-C-0007. Approved for public release, distribution unlimited.

[1] M. Kanda, IEEE Trans. Antennas Propag. **41**, 1349 (1993).
[2] V. Tishchenko, V. Tokatly, and V. Luk'yanov, Measurement Techniques **46**, 76 (2003).
[3] J. Benford, J. A. Swegle, and E. Schamiloglu, *High Power Microwaves* (CRC Press, Boca Raton, 2007).
[4] D. A. Hill, M. Kanda, E. B. Larsen, G. H. Koepke, and R. D. Orr, Generating standard reference electromagnetic fields in the NIST anechoic chamber, 0.2 to 40 GHz, NIST Technical Note 1335, 1990.
[5] K. Matloubi, in *Instrumentation and Measurement Technology Conference, 1993. IMTC/93. Conference Record., IEEE* (IEEE, Piscataway, 1993), pp. 183–184.
[6] J. A. Sedlacek, A. Schwettmann, H. Kübler, R. Löw, T. Pfau, and J. P. Shaffer, Nat. Phys. **8**, 819 (2012).
[7] C. Holloway, J. Gordon, S. Jefferts, A. Schwarzkopf, D. Anderson, S. Miller, N. Thaicharoen, and G. Raithel, IEEE Trans. Antennas Propag. **62**, 6169 (2014).
[8] S. A. Miller, D. A. Anderson, and G. Raithel, New J. Phys. **18**, 053017 (2016).
[9] Y. Jiao, X. Han, Z. Yang, J. Li, G. Raithel, J. Zhao, and S. Jia, Phys. Rev. A **94**, 023832 (2016).
[10] D. A. Anderson, G. A. Raithel, N. Thaicharoen, S. A. Miller, and A. Schwarzkopf, US Patent No. 9,970,973 B2, 2018.
[11] D. H. Meyer, K. C. Cox, F. K. Fatemi, and P. D. Kunz, Appl. Phys. Lett. **112**, 211108 (2018).
[12] A. B. Deb and N. Kjærgaard, Appl. Phys. Lett. **112**, 211106 (2018).
[13] D. A. Anderson, R. E. Sapiro, and G. Raithel, arXiv:1808.08589.
[14] T. Gallagher, *Rydberg Atoms* (Cambridge University Press, New York, 1994).
[15] D. Barredo, H. Kübler, R. Daschner, R. Löw, and T. Pfau, Phys. Rev. Lett. **110**, 123002 (2013).
[16] H. Fan, S. Kumar, H. Kübler, and J. Shaffer, J. Phys. B: Atomic, Mol. Opt. Phys. **49**, 104004 (2016).
[17] J. Grimmel, M. Mack, F. Karlewski, F. Jessen, M. Reinschmidt, N. Sándor, and J. Fortágh, New J. Phys. **17**, 053005 (2015).
[18] D. A. Anderson, E. Paradis, G. Raithel, R. E. Sapiro, and C. L. Holloway, in *2018 11th Global Symposium on Millimeter Waves (GSMM), Boulder, Colorado* (IEEE, 2018), pp. 1–3.
[19] D. A. Anderson and G. Raithel, Appl. Phys. Lett. **111**, 053504 (2017).
[20] C. G. Wade, N. Šibalić, N. R. de Melo, J. M. Kondo, C. S. Adams, and K. J. Weatherill, Nat. Photon. **11**, 40 (2017).
[21] S. Kumar, H. Fan, H. Kübler, A. J. Jahangiri, and J. P. Shaffer, Opt. Exp. **25**, 8625 (2017).
[22] H. Q. Fan, S. Kumar, R. Daschner, H. Kübler, and J. P. Shaffer, Opt. Lett. **39**, 3030 (2014).
[23] C. L. Holloway, J. A. Gordon, A. Schwarzkopf, D. A. Anderson, S. A. Miller, N. Thaicharoen, and G. Raithel, Appl. Phys. Lett. **104**, 244102 (2014).
[24] H. Fan, S. Kumar, J. Sedlacek, H. Kübler, S. Karimkashi, and J. P. Shaffer, J. Phys. B **48**, 202001 (2015).

[25] J. A. Sedlacek, A. Schwettmann, H. Kübler, and J. P. Shaffer, Phys. Rev. Lett. **111**, 063001 (2013).
[26] K.-J. Boller, A. Imamoğlu, and S. E. Harris, Phys. Rev. Lett. **66**, 2593 (1991).
[27] M. Fleischhauer, A. Imamoglu, and J. P. Marangos, Rev. Mod. Phys. **77**, 633 (2005).
[28] A. K. Mohapatra, T. R. Jackson, and C. S. Adams, Phys. Rev. Lett. **98**, 113003 (2007).
[29] D. A. Anderson, S. A. Miller, G. Raithel, J. A. Gordon, M. L. Butler, and C. L. Holloway, Phys. Rev. Appl. **5**, 034003 (2016).
[30] D. Anderson, E. Paradis, and G. Raithel, Appl. Phys. Lett. **113**, 073501 (2018).
[31] D. A. Anderson, A. Schwarzkopf, S. A. Miller, N. Thaicharoen, G. Raithel, J. A. Gordon, and C. L. Holloway, Phys. Rev. A **90**, 043419 (2014).
[32] S. Yoshida, C. O. Reinhold, J. Burgdörfer, S. Ye, and F. B. Dunning, Phys. Rev. A **86**, 043415 (2012).
[33] R. M. Whitley and C. Stroud Jr, Phys. Rev. A **14**, 1498 (1976).
[34] M. G. Bason, M. Tanasittikosol, A. Sargsyan, A. K. Mohapatra, D. Sarkisyan, R. M. Potvliege, and C. S. Adams, New J. Phys. **12**, 065015 (2010).
[35] C. Holloway, M. Simons, J. Gordon, A. Dienstfrey, D. Anderson, and G. Raithel, J. Appl. Phys. **121**, 233106 (2017).
[36] L. Hao, Y. Jiao, Y. Xue, X. Han, S. Bai, J. Zhao, and G. Raithel, New J. Phys. **20**, 073024 (2018).